Structural transition of inversion domain boundaries through interactions with stacking faults in epitaxial GaN

G. P. Dimitrakopulos,[1] Ph. Komninou,[1,*] J. Kioseoglou,[1] Th. Kehagias,[1] E. Sarigiannidou,[1] A. Georgakilas,[2] G. Nouet,[3] and Th. Karakostas[1]

[1]*Physics Department, Aristotle University of Thessaloniki, 540 06 Thessaloniki, Greece*

[2]*FORTH/IESL and Physics Department, University of Crete, 711 10 Heraklion-Crete, P. O. Box 1527, Greece*

[3]*ESCTM-CRISMAT, UMR 6508 CNRS, ISMRA, 6 Boul. Marechal Juin, 14050 Caen Cedex, France*

(Received 26 March 2001; published 6 December 2001)

In epitaxial wurtzite GaN, structural transformations of inversion domain boundaries on prismatic planes are observed at their intersections with stacking faults on the basal plane. High resolution electron microscopy observations show that, following the growth direction, the inversion domain boundaries are transformed from the low-energy and electrically nonactive IDB* type to the high-energy, electrically active, Holt-type structure. By using the topological theory of interfacial defects, it is proved that these transitions are due to the interaction of two distinct planar defects, and can be attributed to the different growth rates of adjacent domains of inverse polarity. The junction lines of the planar defects are characterized by employing the circuit mapping technique as formulated mathematically for multicomponent crystal systems. It is found that these lines exhibit partial dislocation character and an analytical account of such lines is presented.

DOI: 10.1103/PhysRevB.64.245325 PACS number(s): 61.50.Ah, 68.37.Lp, 61.72.Nn, 81.05.Ea

I. INTRODUCTION

GaN epitaxial layers have recently generated significant interest for use in optoelectronic and solid state electronic device applications.[1,2] The material is a III-V semiconductor with large direct band gap, and can be employed for the production of blue and ultraviolet wavelengths. It is challenging that devices comprising this material exhibit satisfactory performance despite a large density and multiplicity of microstructural defects; GaN epitaxial layers bearing the wurtzite crystal structure, commonly contain threading and misfit dislocations, basal and prismatic stacking faults (SF's), nanopipes, and inversion domain boundaries (IDB's).[3–7] The use of different substrates (e.g., sapphire, SiC, Si, GaP, etc.), as well as of different deposition techniques [molecular beam epitaxy (MBE), metal organic chemical vapor deposition (MOCVD), and vapor phase epitaxy (VPE)], has been unsuccessful in preventing the occurrence of such defects in large numbers.[1,7–10] The electronically inert character of many structural defects in GaN has been attributed to the atomic configurations that are associated with them.[11,12] It appears that planar defects in which the atoms are arranged so that ''wrong'' bonds are eliminated, do not induce electronic states in the band gap, and also are energetically favorable compared to defects in which wrong bonds are involved; this is due to the higher ionicity exhibited by GaN as compared to other semiconductors such as GaAs and SiC.

IDB's are particularly important when growth proceeds along a polar direction, since they facilitate the coexistence of crystalline regions of inverse polarity, with a resultant influence on physical and chemical properties such as surface structure and morphology, chemical etching behavior, crystal growth behavior, etc.[7,9,13,14] These defects can be electrically active depending on the atomic coordination along them. IDB's in epitaxial GaN grown along the [0001] direction, commonly appear along $\{10\bar{1}0\}$ prismatic planes,[7,9,15–18] and it has been shown that, for one particular relative displacement of the inverse polarity domains on either side of the boundary, they are electrically inert and energetically favorable.[7,11] Such boundaries have been designated to belong to the IDB* type, are illustrated in Fig. 1(a), and have been observed experimentally.[7,9,15,16,18] In a second configuration, known as Holt-type IDB,[19] the atoms on either side of the boundary are located at interchanged positions in the crystalline structure, as shown in Fig. 1(b). Such IDB's involve wrong bonds and have been shown to be electrically active. Moreover they exhibit a higher formation energy than IDB* ones.[11] Nevertheless, they too have been observed experimentally.[9,15,16] The IDB plane can reside on two locations for each IDB model, i.e., either cutting single bonds (as shown in Fig. 1), or cutting double bonds; the former has been designated as type 1 plane and the latter as type 2.[16] With respect to SF's, it has been shown that they do not introduce localized states in the band gap, although they can bound quantum-well-like regions of sphalerite-structured material in the wurtzite host.[20]

Most published structural results on $\{10\bar{1}0\}$ IDB's in GaN epilayers have been performed on material that had been deposited on (0001) Al_2O_3,[7,9,15–18] and Ruterana *et al.* (Ref. 21) have attributed the introduction of these planar defects to the relief of misfit along [0001] caused by steps and demisteps on the substrate surface. However, they have not been able to conclude that a step leads to a definite model of IDB. Hence the issue concerning the reasons for the introduction of the high-energy Holt IDB's remains unresolved. In a recent presentation,[22] a mechanism for the introduction of Holt IDB's, through the interaction of IDB*'s with I_1 intrinsic basal SF's, was proposed. We hereby give a detailed account of such interactions. In Sec. II, the topological theory of interfacial defects is applied in order to determine *a priori* the character of the IDB-SF junction lines.[23] This analysis results in a thorough and systematic crystallographic description of the IDB-SF interactions. Its results are applied

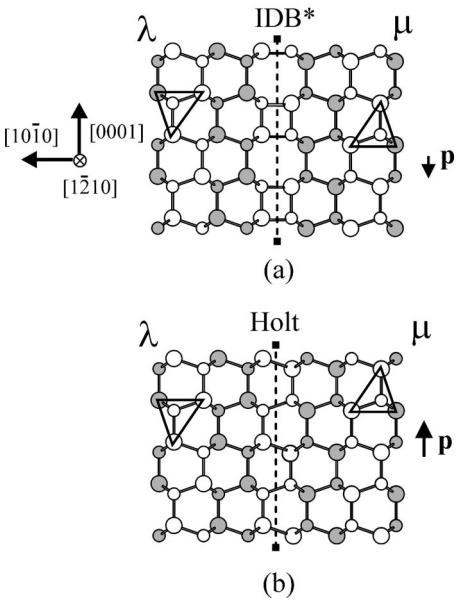

FIG. 1. Schematic illustration of (a) a $\{10\bar{1}0\}$ IDB* planar defect with a relative displacement $\mathbf{p}=-\mathbf{c}/8$ of the abutting domains, and (b) a $\{10\bar{1}0\}$ Holt-type IDB with a relative displacement $\mathbf{p}=3\mathbf{c}/8$ in the GaN structure ($\langle 1\bar{2}10\rangle$ projection, large and small circles denote distinct atomic species, shading denotes levels 0 and $a/2$ along the projection direction, and tetrahedra indicate polarity reversal). The relative displacements are defined taking as reference (zero displacement) the Austerman-Gehman IDB model (Ref. 31). The **p** vectors denote displacement of domain μ with respect to domain λ.

for the interpretation of conventional and high-resolution electron microscopy observations (CTEM and HREM) on GaN epilayers, that are given in Sec. III. The IDB-SF junction lines are characterized on HREM micrographs using circuit mapping. The method is an extension of the Burgers circuit, which was originally introduced by Frank,[24] and has been formulated by Pond and Hirth.[25] This formulation made possible the characterization of interfacial defects including line defects at interface junction lines,[25,26] and it is outlined in the Appendix. Prior to application of the mapping technique, the character of the interfaces that are involved in the interactions is identified by image simulation. The conclusions are discussed in Sec. IV.

II. TOPOLOGICAL ACCOUNT OF IDB-SF INTERACTIONS

Pond and co-workers have presented a rigorous crystallographic framework for the *a priori* topological analysis of interfacial line defects,[23,27] and we apply this method in order to determine the line defects at the IDB-SF junction lines. The method is based on Volterra's description of line defects in elastic continua;[28] this approach is adapted to interfacial defects by considering an initially elastic bicontinuum of two half-spaces, designated λ and μ, that are joined with no initial long-range stresses, as depicted in Fig. 2(a). A ''cut'' is introduced along the interface, and we then modify the exposed surfaces by the addition/removal of material and/or by the application of tractions as shown in Fig. 2(b). After rejoining, a line defect results between the initial interface and the new.

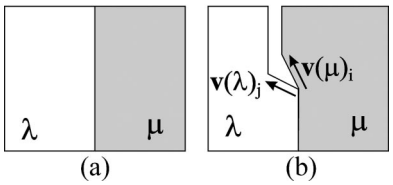

FIG. 2. (a) Bicontinuum. (b) Schematic illustration of the introduction of an interfacial dislocation by the Volterra process.

Assume the new λ surface is obtained from the initial one by the operation $\mathcal{V}(\lambda)_j=(\mathbf{V}(\lambda)_j,\mathbf{v}(\lambda)_j)$ in Seitz notation [where $\mathbf{V}(\lambda)_j$ is the orthogonal part and $\mathbf{v}(\lambda)_j$ the translation part][29] and, similarly, the new μ surface is obtained by $\mathcal{V}(\mu)_i$. Then, by convention, the defect is characterized by the operation required to bring the new μ surface onto the new λ one, i.e., $\mathcal{Z}_{ij}=(\mathbf{Z}_{ij},\mathbf{z}_{ij})=\mathcal{V}(\lambda)_j\mathcal{V}(\mu)_i^{-1}$. For admissible defects, $\mathcal{Z}_{ij}$ describes a rigid-body operation, and, if this is a displacement $\mathcal{Z}_{ij}=(\mathbf{I},\mathbf{z}_{ij})$, where **I** is the identity rotation, then the defect is a dislocation with Burgers vector $\mathbf{b}_{ij}=\mathbf{z}_{ij}$ (other admissible forms are disclinations and dispirations).[23]

In crystals, only symmetry operations leave the respective media invariant; in addition, the lattices introduce natural choices for coordinate frames. With respect to the coordinate frame issue, we choose to define $\mathcal{Z}_{ij}$ in the λ frame, and hence

$$\mathcal{Z}_{ij}=\mathcal{V}(\lambda)_j\mathcal{P}\mathcal{V}(\mu)_i^{-1}\mathcal{P}^{-1}, \tag{1}$$

where $\mathcal{P}=(\mathbf{P},\mathbf{p})$ is the transformation relating the μ frame to the λ one. With respect to the invariance issue, substitution of symmetry operations, designated $\mathcal{W}_i=(\mathbf{W}_i,\mathbf{w}_i)$,[29] in the place of $\mathcal{V}_i$ operations in Eq. (1), gives descriptions of defects between crystallographically equivalent, and hence energetically degenerate, regions. These defects can be obtained *a priori* since the $\mathcal{W}_i$ operations are known. On the other hand, if at least one of the operations substituted in Eq. (1) is not a symmetry operation, the defect separates crystallographically distinct regions. In the latter case, if there are no constraints on the $\mathcal{V}_i$ operations, we cannot predict which defects are physically feasible. Nevertheless, at certain instances, there are structural choices of $\mathcal{V}_i$ operations, and Eq. (1) defines the rigorous framework in which to investigate the corresponding defects. This is particularly relevant for the issue at hand, i.e., the IDB-SF interactions, as discussed below.

As shown in Fig. 2(b), interfacial line defects can have an associated step character, and the Volterra approach takes into account the incompatibilities between steps on abutting surfaces. In the following we take our interface to be a $\{10\bar{1}0\}$ IDB, and we will examine the defect character of line junctions with SF's. For this purpose, we will consider SF-introducing $\mathcal{V}_i$ operations with related steps.

The wurtzite structure (spacegroup $P6_3mc$) can be considered as being composed of two interpenetrating hcp substructures that are displaced by $\frac{3}{8}[0001]$, and each comprises

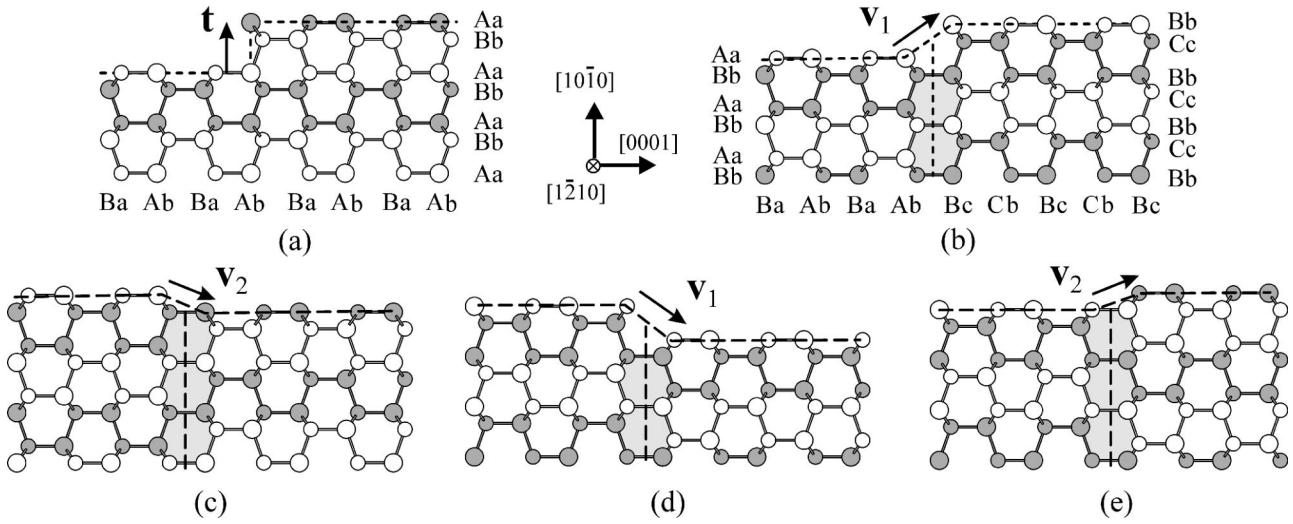

FIG. 3. (a) Schematic illustration of a step $h=\sqrt{3}a/2$ between unrelaxed crystallographically equivalent $\{10\bar{1}0\}$ surface regions; the step corresponds to a lattice translation $\mathbf{t}=\frac{1}{3}[2\bar{1}\bar{1}0]$. (b)–(e) Schematic illustrations of steps on an unrelaxed $\{10\bar{1}0\}$ surface due to the impingement of a I_1 SF. The step vectors and heights are as follows. (b) $\mathbf{v}_1=\frac{1}{6}\langle 20\bar{2}3\rangle$, $h_1=\sqrt{3}a/3$, (c) $\mathbf{v}_2=\frac{1}{6}\langle\bar{2}203\rangle$, $h_2=-\sqrt{3}a/6$, (d) $\mathbf{v}_1=\frac{1}{6}\langle\bar{2}023\rangle$, $h_1=-\sqrt{3}a/3$ (e) $\mathbf{v}2=\frac{1}{6}\langle 2\bar{2}03\rangle$, $h_2=\sqrt{3}a/6$. (Atoms are as in Fig. 1. In (a) and (b), the stacking sequences along [0001] and $\langle 10\bar{1}0\rangle$ have been indicated.)

distinct atomic species. The stacking sequence along [0001] is $\ldots AaBbAaBb\ldots$ i.e., each layer parallel to the basal plane is composed of two sublayers of distinct atomic species. As a result of the interpenetration, half of the symmetry operations that describe the hcp structure are suppressed in wurtzite. Consequently, crystallographically equivalent $\{10\bar{1}0\}$ surface regions, at different levels along $\langle 10\bar{1}0\rangle$, can only coexist through steps corresponding to lattice translations such as $\mathcal{W}_i=(\mathbf{I},\mathbf{t}_i)=(\mathbf{I},\frac{1}{3}\langle 2\bar{1}\bar{1}0\rangle)$; these vectors connect Aa to Aa and Bb to Bb layers, as illustrated in Fig. 3(a). Such steps have heights that are integer multiples of $h=\sqrt{3}a/2$ (where a is the GaN lattice parameter in the basal plane).

Figures 3(b) to 3(e) depict the impingement of a I_1 intrinsic basal SF on a $\{10\bar{1}0\}$ surface. This fault corresponds to one violation of the stacking rule or, equivalently, to the introduction of one row of sphalerite stacking in the wurtzite stacking sequence along [0001], and can be considered to have been formed by the removal of one basal layer (e.g., Aa) followed by a $\frac{1}{3}\langle 10\bar{1}0\rangle$ shear. This leads to the stacking: $\ldots AaBbAaBbCcBbCc\ldots$, and the corresponding displacement vector is $\frac{1}{6}\langle 20\bar{2}3\rangle=\frac{1}{3}\langle 10\bar{1}0\rangle+\frac{1}{2}[0001]$. As the removal of a double layer is required, the I_1 SF is a growth defect.[30] Its effect on a $\{10\bar{1}0\}$ surface depends upon the sense of the sphalerite units. For each sense (i.e., either towards or away from the interface), two step-introducing operations can be distinguished; these are $\mathcal{V}_1=(\mathbf{I},\mathbf{v}_1)=(\mathbf{I},\pm\frac{1}{3}\langle 10\bar{1}0\rangle+\frac{1}{2}[0001])$ and $\mathcal{V}_2=(\mathbf{I},\mathbf{v}_2)=(\mathbf{I},\pm\frac{1}{6}\langle\bar{1}010\rangle+\frac{1}{2}[0001]\pm\frac{1}{6}\langle\bar{1}2\bar{1}0\rangle)$ (the signs of the $\langle 10\bar{1}0\rangle$ components are reversed when changing the sense of the sphalerite units). The corresponding step heights are $h_1=\pm\sqrt{3}a/3$ and $h_2=\pm\sqrt{3}a/6$. We note that the surfaces on either side of these steps are energetically degenerate even though they are not crystallographically equivalent. We also note that the steps given in Fig. 3 are the smallest possible; all other feasible steps can be regarded as combinations of these.

Similarly to hcp, a second type of intrinsic SF, that is termed I_2, comprises two rows of sphalerite stacking formed by a $\frac{1}{3}\langle 10\bar{1}0\rangle$ shear. However, we concentrate on the I_1 SF's due to the $\frac{1}{2}[0001]$ component. In an earlier publication,[22] it was proposed that this component could accommodate the coexistence of the two principal $\{10\bar{1}0\}$ IDB types, i.e., IDB* and Holt, that have been illustrated in Fig. 1. Indeed, the relative displacements of the inverse polarity domains are $-\frac{1}{8}[0001]$ and $\frac{3}{8}[0001]$, respectively, for the two IDB structures, taking as reference the unrelaxed, or Austerman-Gehman IDB model (this is the model in which one hcp substructure remains undeviated while the other switches its tetrahedral site upon crossing the boundary).[31] Initial observations for such IDB*-Holt transformations were given in Ref. 22. In the present work, we undertake an extensive and thorough investigation of the IDB-I_1 SF interactions.

By employing the steps depicted in Fig. 3, we list in Fig. 4 all the possible interactions of a IDB* with a I_1 SF leading to a Holt IDB. These interactions and the corresponding defects have been obtained using the above outlined Volterra approach and Eq. (1). The inverse polarity domains have been designated λ and μ. The orthogonal part of the transformation $\mathcal{P}$ is $\mathbf{P}=\bar{\mathbf{1}}$, the inversion operation, and the displacement $\mathbf{p}$ is defined by the IDB type prior to the Volterra cut. It can be seen that the dislocations at the junction lines have an associated step, the height of which is given by the average of the step heights on the abutting surfaces. The $\frac{1}{2}[0001]$ component of the SF translation has been employed for the IDB structure transformation. In Figs. 4(a), 4(b), 4(e), and 4(f), the SF terminates on a flat λ surface whereas, in the rest, the λ surface exhibits a step of the same sense. (Juxta-

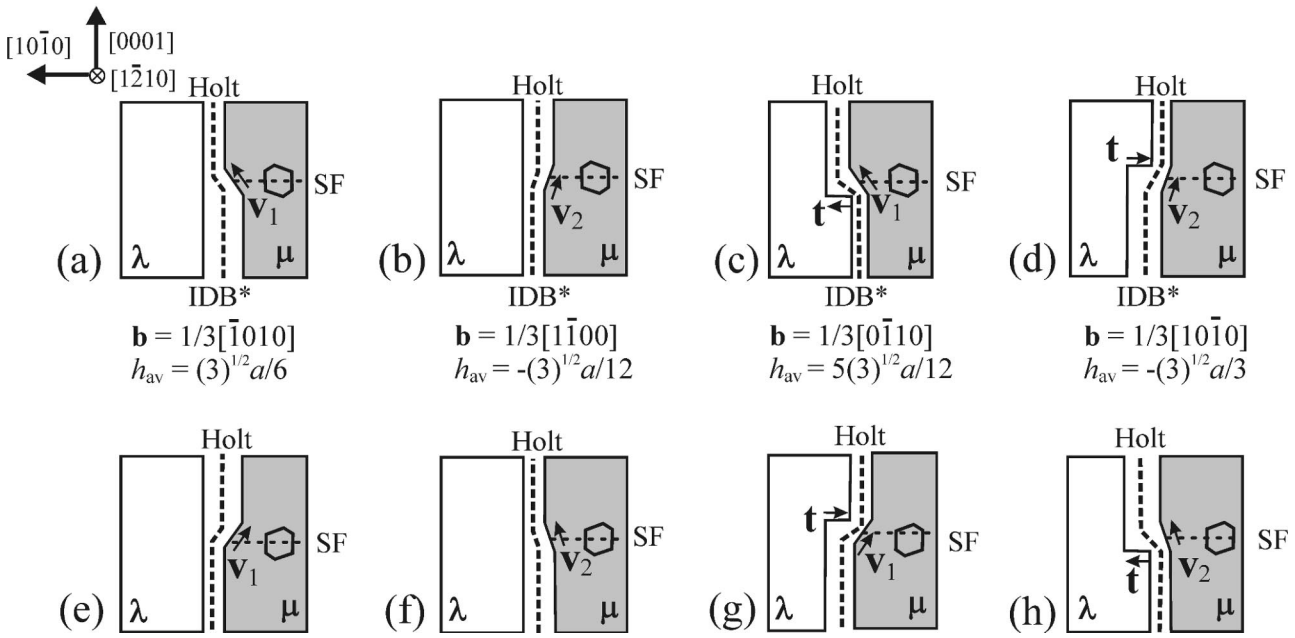

FIG. 4. The possible IDB*-I_1 SF interactions, leading to a Holt IDB. The interactions are illustrated using Volterra drawings. The IDB and SF have been indicated by broken lines. On the SF, a sphalerite unit has been drawn to indicate its sense. The step vectors are as given in Fig. 3. In (a) to (d) the configurations with the sense towards the IDB are given, and in (e) to (h) the sense is away from the IDB. The given configurations correspond to minimum Burgers vectors and minimum average step heights (h_{av}).

posed steps of opposite senses have not been considered since they lead to relatively large Burgers vectors.) The configurations given in Fig. 4 correspond to minimum Burgers vectors and minimum steps, and other configurations arising as a combination of these are conceivable.

In addition, Fig. 5 lists all the configurations in which the I_1 SF crosses into the inverse polarity domain; in these, the IDB structure is not transformed. In Figs. 5(a) and 5(b) it can be seen that the SF can cross via a defect free step. However, if the sense of the sphalerite units adopts a mirror-related orientation with respect to the IDB plane, then a partial dislocation with [Fig. 5(c)] or without [Fig. 5(d)] an associated step is required. In Fig. 5 the IDB structure is conserved because the SF type is conserved as well. We could also imagine that the I_1 SF emerges as I_2 after the IDB. In that case, the $\frac{1}{2}[0001]$ component would have been absorbed by a structural transformation of the IDB from IDB* to Holt or vice versa.

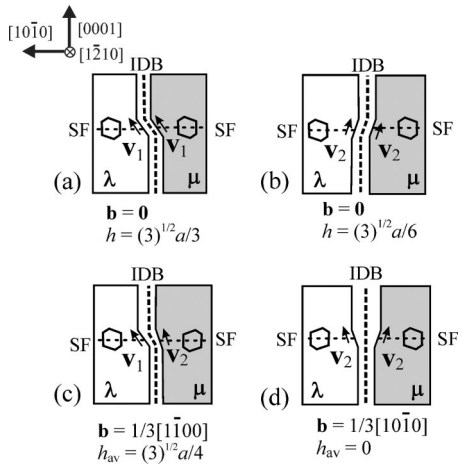

FIG. 5. Volterra drawings illustrating the crossings of an IDB by a I_1 SF. The IDB structure is conserved in the interactions. In (a) and (b) the sphalerite units on either side of the IDB have the same sense, and in (c) and (d) they have mirror-related senses. The latter configurations require a partial dislocation.

Aside from the configurations and transformations given in Figs. 4 and 5, one can imagine IDB configurations that are not related to a SF. For example, in the interactions depicted in Figs. 4 and 5, the IDB plane type has been kept invariant, i.e., either type 1 or type 2. The transformations IBD*1-IDB*2 and Holt1-Holt2, in which the location of the IDB plane changes from crossing single bonds to crossing double bonds, do not necessitate a partial dislocation since the dichromatic complex (Ref. 23) is the same for 1- and 2-type boundaries. Such defect-free transformations have been observed experimentally.[16]

In the above, a rigorous analysis of IDB interactions with I_1 SF's has been given. In the following we proceed to study these in experimental HREM images, and to analyze the observed interactions. For the analysis the circuit mapping technique will be employed (see the Appendix).

III. EXPERIMENTAL OBSERVATIONS AND ANALYSIS

GaN layers were epitaxially deposited on (0001) Al_2O_3 by rf plasma MBE. Prior to deposition, the sapphire surface had undergone nitridation at 723 K, followed by low-T deposition of a 8–20 nm AlN buffer. Following a high-T annealing of the buffer layer, GaN epilayers were grown under various conditions. After deposition, the epilayers exhibited the wurtzite structure and the relative orientation relationship

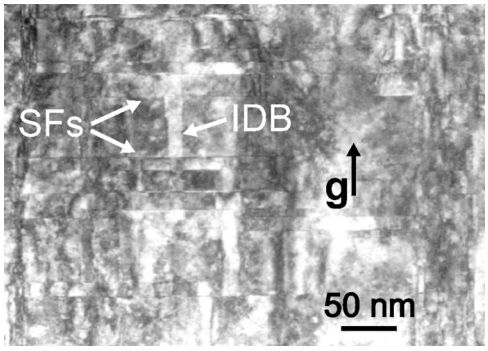

FIG. 6. Multiple-beam, dark-field TEM micrograph in cross-section geometry, of the epitaxial GaN film, viewed with the 0002 reflection. The image depicts a large density of basal SF's interacting with $\{10\bar{1}0\}$ IDB's. Under the present diffracting condition, edge-type threading dislocations are in extinction. The SF's that are visible are intrinsic I_1 SF's, as well as few extrinsic E SF's.

with the sapphire substrate was $(0001)\mathrm{GaN}//(0001)\mathrm{Al_2O_3}$, $\langle 10\bar{1}0\rangle \mathrm{GaN}//\langle 1\bar{2}10\rangle\ \mathrm{Al_2O_3}$. Sample preparation for $[1\bar{2}10]$ cross-section electron microscopy (XTEM) involved mechanical thinning followed by ion milling to electron transparency. For the observations, a Topcon 002B HREM, operated at 200 kV, with a point to point resolution of 0.18 nm and $C_s = 0.4$ mm, and a JEOL JEM 120CX TEM were employed. Image simulations of the defects on HREM micrographs were performed using the multislice algorithm in the EMS software.[32] For this purpose, supercells for the defects were created in $[1\bar{2}10]$ projection. Series of simulated images of all the IDB and SF structural models from -29 to -69 nm defocus values (step 2 nm), and for thickness from 0.32 nm (i.e., equal to one lattice parameter a) to 14.4 nm (step 0.16 nm) were constructed. Prior to comparison with the simulations the experimental conditions of thickness and defocus were determined by calculating the map of through defocus-thickness simulated images of perfect GaN.

Figure 6 is a conventional XTEM micrograph, illustrating a characteristic overall view of the GaN thin film. It can be seen that a multiplicity of interacting extended defects, basal SF's and $\{10\bar{1}0\}$ IDB's, exists. Under the particular diffraction conditions (multiple-beam dark-field with the $\mathbf{g}=0002$ reflection), inversion domains are distinguished by the change in the mean intensity level.[33] In addition, the majority of threading dislocations, i.e., dislocations with Burgers vector $\mathbf{b}=\frac{1}{3}\langle\bar{2}110\rangle$, are in extinction. Image simulations on a number of HREM micrographs have shown that the majority of IDB's are IDB* defects with occasional Holt-type defects; in addition, it has been shown that most basal SF's are of intrinsic character.[4,9] Both I_1 and I_2 SF's are low-energy defects since they do not disturb nearest-neighbor packing, with I_1 being the most energetically favorable.[20] However, based on the relevant SF displacements given in Sec. II, it is deduced that the intrinsic SF's that are visible with the 0002 reflection in Fig. 6 are I_1 SF's.

In the HREM micrograph of Fig. 7, an interaction between a I_1 SF and a narrow inversion domain, bounded by two IDB's, is illustrated. The IDB's and the SF were characterized by comparison with corresponding simulated images. For the particular imaging conditions (i.e., defocus corresponding to the first maximum of contrast), tunnels in the structure are projected onto white spots and, for the Holt model, the stacking sequences on either side of the IDB appear to have same sense, whereas, for IDB*, the senses appear opposite.[16] Hence the two models can be distinguished. Also, in Fig. 7 it is observed that the IDB planes are traced onto white spots which, for this defocus, corresponds to the IDB plane cutting single bonds; hence these are type-1 boundaries as explained in the introduction and depicted in Fig. 1. Following the identification of the planar defects, we move on to study their interactions. Starting the description from the right-hand side of the image, the SF is observed initially to cross an IDB*; this constitutes the first interaction and the cases of Fig. 5 are applicable. The SF then stops on the second IDB, thereby inducing a transformation of IDB character from IDB* to Holt type; this is the second interaction, and the cases of Fig. 4 are applicable.

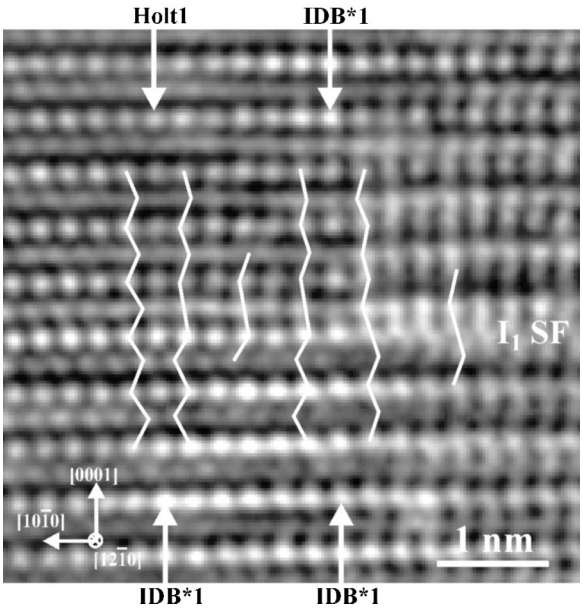

FIG. 7. Cross-section HREM micrograph along $[1\bar{2}10]$, showing a I_1 SF interacting with two IDB's that bound a narrow inverse polarity domain. Starting the description from the right-hand side of the image, the SF crosses an IDB*1 defect and then stops on the second IDB, transforming its structure from IDB*1 to Holt1. The arrows indicate the IDB planes. Stacking sequences at the matrix material and the inverse polarity domain have also been indicated (defocus $= -29$ nm, tunnels are on white spots).

In order to characterize the first interaction (junction 1-Jn1), we observe, from Fig. 7, that the SF-associated sphalerite stacking continues after crossing the IDB without changing its sense. This immediately excludes the cases of Figs. 5(c) and 5(d). Then, if we also consider the observed step height of the IDB plane at the IDB-SF junction line, it appears that Fig. 5(b) is the most probable. However, further simulations are necessary, and this is undertaken below.

Image simulations of structural models of the first interaction were performed and, for this purpose, appropriate supercells were created. Since no relaxation algorithms were

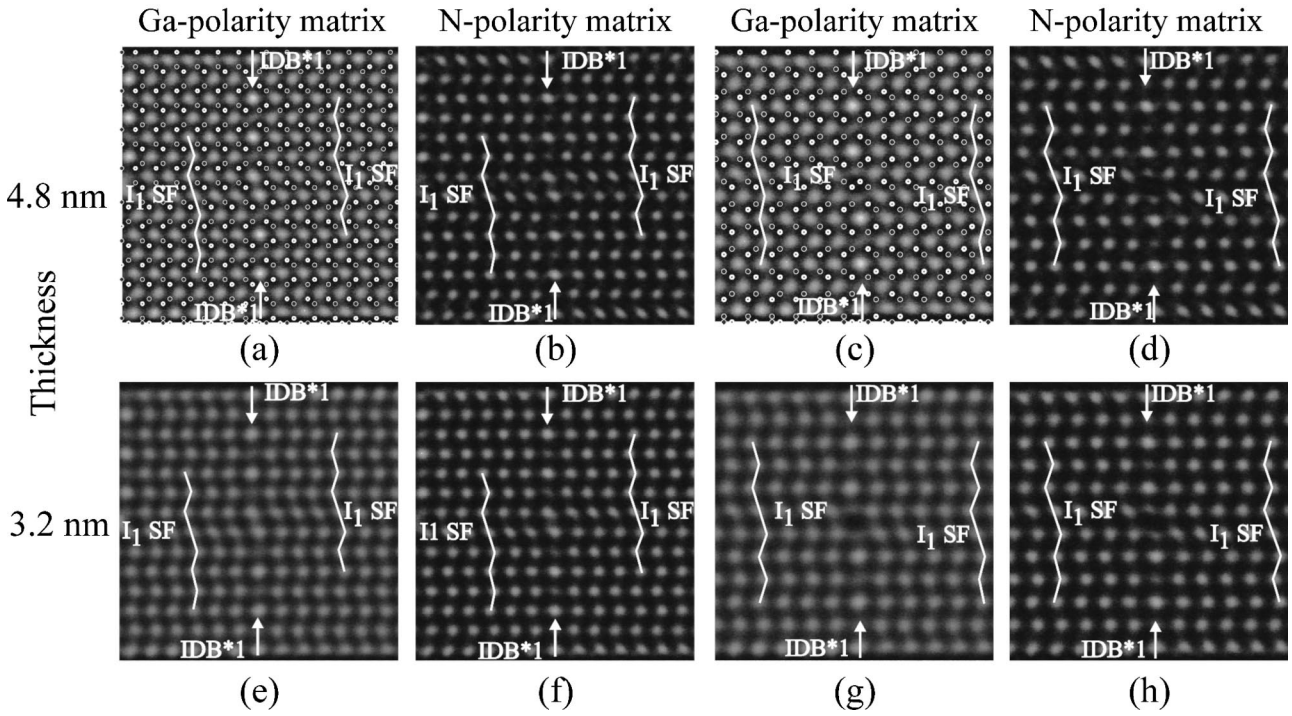

FIG. 8. HREM image simulations along $[1\bar{2}10]$, corresponding to the IDB-SF interaction of Fig. 5(b). The simulations were performed with defocus $=-29$ nm (first maximum of contrast), and two levels of specimen thickness are illustrated. The matrix material (depicted on the right-hand side of the IDB plane) can be either Ga polarity [(a), (c), (e), (g)] or N polarity [(b), (d), (f), (h)], and the SF-associated stacking can be shifted by either $-\mathbf{c}/2$ [(a), (b), (e), (f)] or $+\mathbf{c}/2$ [(c), (d), (g), (h)] in the inverse domain with respect to the matrix. The arrows indicate the IDB planes; the stacking sequences on either side of the IDB's are also shown. In (a) and (c), the atomic positions of the distinct atomic species, depicted as open and full circles, have been superimposed on the images.

available, the IDB-SF junction line was kept unrelaxed in these cells. However, the simulations accurately depict the relative orientations and senses of the stacking sequences. Four supercells were simulated for each of the two possible cases, i.e., Figs. 5(a) and 5(b). This is because there are two possible ways of arranging the polarities and two ways of arranging the sphalerite row before and after the IDB. With respect to the polarities, we can choose the matrix material to be Ga polarity, and the inverse domain *N* polarity, or vice versa. (Note that, by convention, ''Ga polarity'' corresponds to [0001] being along the Ga-N bond.[7,16]) Also the IDB step shifts the sphalerite row by either $+\mathbf{c}/2$ or $-\mathbf{c}/2$, and this results in the second pair of supercells. A comparison between the experimental micrograph and the simulations has led to the conclusion that Fig. 5(b) is the case that best describes $Jn1$. The corresponding simulated images are given in Fig. 8 for two levels of specimen thickness that match the experimental conditions, while those of Fig. 5(c) are not listed for brevity. From the simulated images it has also been concluded that the sphalerite row shifts by $+\mathbf{c}/2$ inside the inverse polarity domain, on account of the interaction. However, the polarity issue cannot be clarified since, at this defocus, the images remain unaffected by polarity reversal. Also, variations of specimen thickness do not appear to affect the image.

Figure 9 is a HREM experimental micrograph of the same area as Fig. 7, for imaging conditions corresponding to the second maximum of contrast. At these conditions, atomic columns are projected onto white spots; hence circuit mapping is facilitated, whereas the imaging conditions of Fig. 7 aided the characterization of the planar defects and their steps. In Fig. 9, the stacking sequences on either side of the IDB's are in agreement with the observations of Potin *et al.* for this contrast maximum,[16] i.e., they appear to have the same sense for the IDB* and opposite senses for Holt. Hence the identification of the IDB's in Fig. 7 is further confirmed. However, it is now observed that no shift of the SF-associated stacking is discernible. Due to this, another series of image simulations was undertaken for this maximum, in order to positively identify the positions of the faults and the correspondence with the structural model. These simulations are illustrated in Fig. 10 for the case at hand, i.e., that of Fig. 5(b) with a $+\mathbf{c}/2$ shift. The calculations show that, at this defocus, the apparent shift of the sphalerite row varies depending on both the polarity and specimen thickness. In particular, if the matrix material is Ga polarity, the apparent shift changes from 0 to **c** after approximately five lattice periodicities, as shown in Figs. 10(a) and 10(c). On the other hand, a *N*-polarity matrix always gives an apparent shift equal to **c**, irrespective of specimen thickness, as shown in Figs. 10(b) and 10(d). Hence we conclude that our observations are consistent with Ga-polarity matrix material, in agreement with results published earlier for these specimens.[9] In addition, a one-to-one correspondence between atomic columns in the image and the structural model is established; this structural model is then used as reference space for circuit mapping in

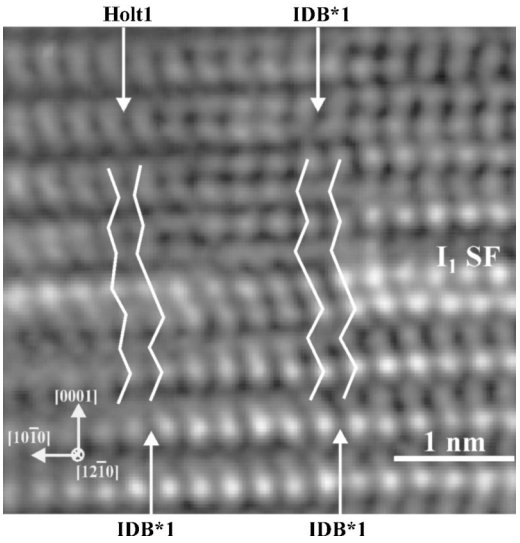

FIG. 9. HREM micrograph of the same area as Fig. 7 at the second maximum of contrast (defocus $=-59$ nm, atoms are on white spots). No shift of the SF-associated stacking is observed in the inverse polarity domain with respect to its location in the matrix. The arrows indicate the IDB planes and the stacking sequences on either side of the IDB's are also shown.

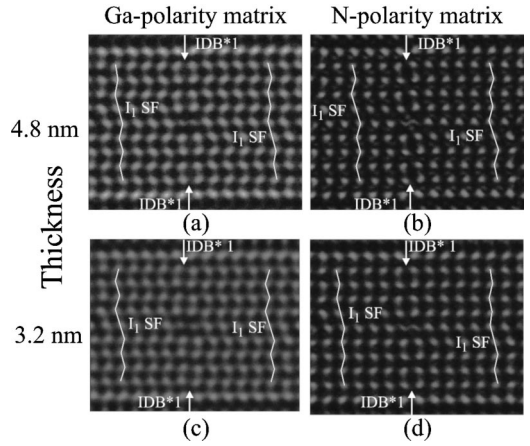

FIG. 10. HREM image simulations along $[1\bar{2}10]$, corresponding to the IDB-SF interaction of Fig. 5(b). The simulations were performed with defocus $=-59$ nm (second maximum of contrast), and two levels of specimen thickness are illustrated. The matrix can be either Ga polarity [(a), (c)] or N polarity [(b), (d)]. In the structural model employed for the simulations, the SF-associated stacking has been taken to undergo a $+\mathbf{c}/2$ shift in the inverse domain on account of the SF's interaction with the IDB*1. It is observed that the apparent shift of this stacking depends on both the polarity and specimen thickness. The arrows indicate the IDB planes and stacking sequences on either side of the IDB's are shown.

order to characterize the IDB-SF junction line, as described below.

The zero defect character of the $Jn1$ line, that has been predicted in Fig. 5(b), can be confirmed by employing the circuit mapping technique in the manner described in the Appendix for multicomponent systems. Figure 11(a) is the same micrograph as Fig. 9 except that closed circuits have been indicated around the two junction lines. These circuits are shown mapped in the appropriate reference space in Figs. 11(b) and 11(c). The crystal components have been distinguished in Fig. 11(a) by designating them as λ, μ, and κ, where λ and κ correspond to the matrix material and μ to the inverse domain. The closed circuit $sghijklmnpqrs$ around $Jn1$ is shown mapped in the reference space in Fig. 11(b) whereby no closure failure arises. The appropriate multicomponent reference space for mapping has been identified by the image simulations of Figs. 8 and 10. We note that care should be exercised when crossing the IDB's. This is because, in materials exhibiting hexagonal close packing, the centers of inversion are not located at atomic sites. When crossing an IDB, inversion operations have to be performed using such centers, and they have to be followed by the rigid-body translation of the corresponding IDB model. This is illustrated in Figs. 11(b) and 11(c) by enlargements of the IDB crossing locations. Moreover, we need to consider that wurtzite is composed of two interpenetrating hcp substructures. Hence, when mapping the circuit, we need to exercise care in order to employ the inversion centers of the appropriate substructure, i.e., those of the hcp substructure corresponding to the atomic sites that are used for mapping the circuit segments. The zero Burgers vector of $Jn1$ is further verified if we formulate the circuit mathematically. The circuit segments are as follows:

$$sgh{:}\mathcal{C}(\kappa)_1=(\mathbf{I},2[0001])(\mathbf{I},2[\bar{1}010]), \tag{2a}$$

$$ijk{:}\mathcal{C}(\kappa)_2=\left(\mathbf{I},\frac{1}{3}[2\bar{1}\bar{1}0]\right)(\mathbf{I},2[10\bar{1}0])(\mathbf{I},2[0001]), \tag{2b}$$

$$lmn{:}\mathcal{C}(\mu)_2=(\mathbf{I},[0001])(\mathbf{I},[\bar{1}010]), \tag{2c}$$

$$pqr{:}\mathcal{C}(\mu)_1=\left(\mathbf{I},\frac{1}{3}[2\bar{1}\bar{1}0]\right)(\mathbf{I},[10\bar{1}0])(\mathbf{I},3[0001]) \tag{2d}$$

(note that sequences of Seitz operations are read from right to left). In addition, the rigid-body translation vectors that are associated with crossing the planar defects are $\mathbf{p}(\kappa)_{\mathrm{SF}}=\frac{1}{6}[\bar{2}023]$, $\mathbf{p}_{\kappa\mu}=\frac{1}{8}[0001]$, $\mathbf{p}(\mu)_{\mathrm{SF}}=\frac{1}{6}[\bar{2}023]$, $\mathbf{p}_{\mu\kappa}=\frac{1}{8}[000\bar{1}]$. Similar to Eq. (A1) of the Appendix, the composite circuit operator for $Jn1$ is given by the equation

$$\mathcal{C}(\kappa\mu)=(\mathbf{I},\mathbf{p}_{\mu\kappa})\mathbf{P}\{\mathcal{C}(\mu)_1(\mathbf{I},\mathbf{p}(\mu)_{\mathrm{SF}})\mathcal{C}(\mu)_2\}\mathbf{P}^{-1}(\mathbf{I},\mathbf{p}_{\kappa\mu}) \times\mathcal{C}(\kappa)_2(\mathbf{I},\mathbf{p}(\kappa)_{\mathrm{SF}})\mathcal{C}(\kappa)_1. \tag{3}$$

In Eq. (3) the circuit operator is expressed in the frame of domain κ. Substitution of the operators given in Eq. (2) yields $\mathcal{C}(\kappa\mu)=(\mathbf{I},\mathbf{0})$, identifying $Jn1$ as a dislocation-free IDB-SF interaction.

Following the characterization of the IDB-SF interaction of $Jn1$, we proceed with $Jn2$, whereby the SF stops on the IDB and transforms its structure as shown in the experimental micrograph of Figs. 7 and 9. The previous analysis has already identified the sense of the SF-associated sphalerite row, and this immediately excludes the cases depicted in

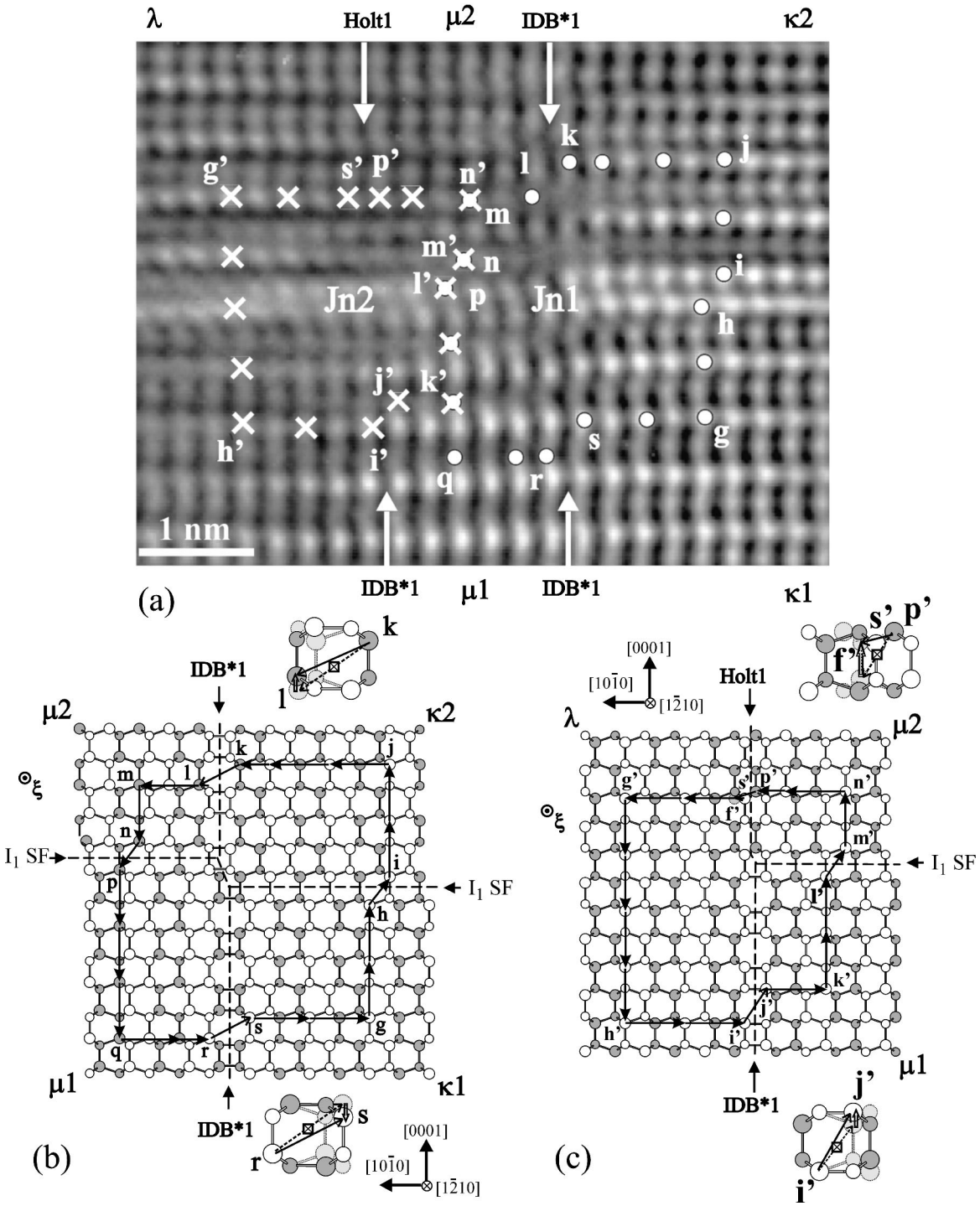

FIG. 11. (a) The same micrograph as in Fig. 9 with closed circuits $sghijklmnpqrs$ and $s'g'h'i'j'k'l'm'n'p's'$ drawn around the IDB-SF junction lines, $Jn1$ and $Jn2$, respectively. (b) Mapping of circuit $sghijklmnpqrs$ around $Jn1$ to the reference space. Enlargements are used to make clear the appropriate way to cross the IDB's using inversion centers (depicted as cross-hatched rectangles) and rigid-body translations in the complex of interpenetrating crystals (see text). (c) Mapping of circuit $s'g'h'i'j'k'l'm'n'p's'$ around junction $Jn2$ to the reference space; closure failure **fs** arises. The line defect accommodates the transition from IDB*1 to Holt1. ($\vec{\xi}$ denotes the line directions of the defects. Atoms are as in Fig. 1.)

Figs. 4(a)–4(d). In addition, the cases depicted in Figs. 4(g) and 4(h) are associated with a relatively large step of the IDB plane, which is not observed. The remaining cases are those of Figs. 4(e) and 4(f), which correspond to lines exhibiting edge and mixed dislocation character, respectively. In Fig. 11(a), a closed circuit $s'g'h'i'j'k'l'm'n'p's'$ has been drawn around $Jn2$, and it is shown mapped in the complex of interpenetrating crystals in Fig. 11(c), where it is observed

that closure failure **FS** arises; this identifies $Jn2$ as a dislocation line. The Burgers vector is determined if we formulate the circuit mathematically; the circuit segments are

$$s'g'h'i':\mathcal{C}(\lambda)=(\mathbf{I},2[\bar{1}010])(\mathbf{I},4[000\bar{1}])(\mathbf{I},2[10\bar{1}0]), \tag{4a}$$

$$j'k'l':\mathcal{C}(\mu)_1=(\mathbf{I},2[000\bar{1}])(\mathbf{I},[10\bar{1}0]), \tag{4b}$$

$$m'n'p':\mathcal{C}(\mu)_2=\left(\mathbf{I},\frac{1}{3}[\bar{2}110]\right)(\mathbf{I},[\bar{1}010])(\mathbf{I},[000\bar{1}]). \tag{4c}$$

Also the rigid-body translations associated with crossing the planar defects are $\mathbf{p}_{\lambda\mu}=\frac{1}{8}[0001]$ $\mathbf{p}_{\mathrm{SF}}=\frac{1}{6}[20\bar{2}3]$ and $\mathbf{p}_{\mu\lambda}=\frac{3}{8}[0001]$. The composite circuit operator for $Jn2$ is given by Eq. (A1), and substitution yields $\mathcal{C}(\lambda\mu)=(\mathbf{I},\frac{1}{3}[1\bar{1}00])$ identifying $Jn2$ as a partial dislocation of mixed type with Burgers vector $\mathbf{b}^{Jn2}=\frac{1}{3}[\bar{1}\bar{1}00]$ expressed in the λ coordinate frame. In conclusion, the junction line that accommodates the IDB*1-Holt1 transformation corresponds to the configuration depicted in Fig. 4(f) and is accommodated by a dislocation of mixed type. The crossing of the IDB*1 by a I_1 SF corresponds to the configuration of Fig. 5(b), and is accommodated without a dislocation.

In the above, junction lines between a I_1 SF and IDB's bounding a narrow inverse polarity domain were presented. In the following, we present, for completeness, interactions between I_1 SF's and IDB's bounding a relatively wide inverse domain. For brevity, the circuits will only be illustrated in graphical form, omitting the analytical mathematical calculations. Figure 12(a) is a HREM micrograph showing an inverse polarity domain with an internal I_1 SF. On the left-hand side, the SF terminates on the IDB and transforms it from IDB*1 to Holt1 (junction $Jn3$). On the right-hand side, the SF accommodates a Holt2 to IDB*1 transformation (junction $Jn4$). The Holt2 IDB is itself a product of the interaction of an external I_1 SF with a IDB*2 (junction $Jn5$). The occurrence of the Holt2 segment is interesting since double ''wrong'' bonds are involved; such IDB's have also been observed by Potin *et al.*[16] The external SF terminates at a partial dislocation. All the IDB-SF interactions induce steps on the IDB plane. No IDB crossings by SF's are observed in this micrograph.

In Fig. 12(a) the IDB's and SF's have been characterized by the comparison with simulated images that are given as insets. In addition, closed circuits have been drawn around all the IDB-SF junctions in order to identify their defect character; these circuits are shown mapped in the reference space in Figs. 12(b) to 12(d). The circuit around $Jn3$ characterizes the line as a mixed partial dislocation with Burgers vector $\mathbf{b}^{Jn3}=\frac{1}{3}[\bar{1}100]$, that corresponds to the case depicted in Fig. 4(f). The case of $Jn4$ is rather more complex in that there is a structural transformation from Holt to IDB* as well as a change of IDB plane from type 2 to type 1. We can consider these to be two discrete and consecutive transformations, for example Holt2-to-Holt1-to-IDB*1. As mentioned in Sec. II, a dislocation-free step is required to transform Holt2 to Holt1. In addition, a partial dislocation is required to transform Holt1 to IDB*1. This agrees with the result of circuit mapping that yields $\mathbf{b}^{Jn4}=\frac{1}{3}[1\bar{1}00]$ and corresponds to the case of Fig. 4(f). The associated step of the IDB plane has height equal to $3\times\sqrt{3}a/12$, which is the sum of the step corresponding to the case of Fig. 4(f), plus the dislocation-free step that changes the IDB plane from type 2 to type 1. The last junction line is $Jn5$, and the corresponding Burgers vector is $\mathbf{b}^{Jn5}=\frac{1}{3}[\bar{1}010]$, i.e., the dislocation is edge type; the relevant case is Fig. 4(a). We note that all Burgers vectors have been expressed in the coordinate frame of domain λ (or, equivalently, domain κ). In concluding this section, we remark that, out of eight predicted IDB* to Holt transformations through defects, two have been illustrated here, i.e., those of Figs. 4(a) and 4(f). In addition, out of four conceivable IDB crossings by the I_1 SF, one has been illustrated, i.e., that of Fig. 5(b).

IV. DISCUSSION AND CONCLUSIONS

A detailed study of the interactions between I_1 SF's and IDB's has been presented using HREM observations and a rigorous topological analysis. The observations have been compared with extensive image simulations and the defect character of the IDB-SF junction lines has been determined using circuit mapping. It has been observed, in a number of instances, that the I_1 SF's are defects that can interact with IDB's thereby introducing structural transformations, from the low energy and electrically nonactive IDB* to the electrically active and high energy Holt IDB or vice versa. These IDB-SF junction lines have partial dislocation character with $\mathbf{b}=\frac{1}{3}\langle 10\bar{1}0\rangle$. The Burgers vectors of such partials are in the SF plane, whereas the $\frac{1}{2}[0001]$ component is absorbed by the IDB structure transformation. A subtle point is made, i.e., that a $\frac{1}{2}[0001]$ partial plus an IDB* is topologically and structurally equivalent to a Holt IDB. Also, at one instance where the inverse polarity domain was relatively narrow, it was observed that the I_1 SF crossed one IDB without affecting its structure, and that this junction line did not exhibit defect character.

Our results are at variance to the conclusion of Potin *et al.* (Ref. 16) that IDB*'s do not switch to Holt IDB's. However, we agree that the growth conditions are responsible for the introduction of the Holt defects but, in our specimens, this is done in an indirect way, i.e., through the introduction of I_1 SF's. It is therefore proposed that finding ways to reduce the density of I_1 SF's could lead to GaN epilayers of improved properties. In addition to the I_1 SF's, the extrinsic (E-type) SF's have a $\frac{1}{2}[0001]$ rigid-body translation, and could also introduce IDB structural transformations, but these defects occur in much smaller numbers. It has also been observed that, if the SF crosses the IDB, then the interaction is harmless in that no IDB structural transformation results. Therefore, a second way to improve epilayer properties would be to facilitate these crossings over the SF terminations on IDB walls.

However, the conditions, under which a SF can cross an

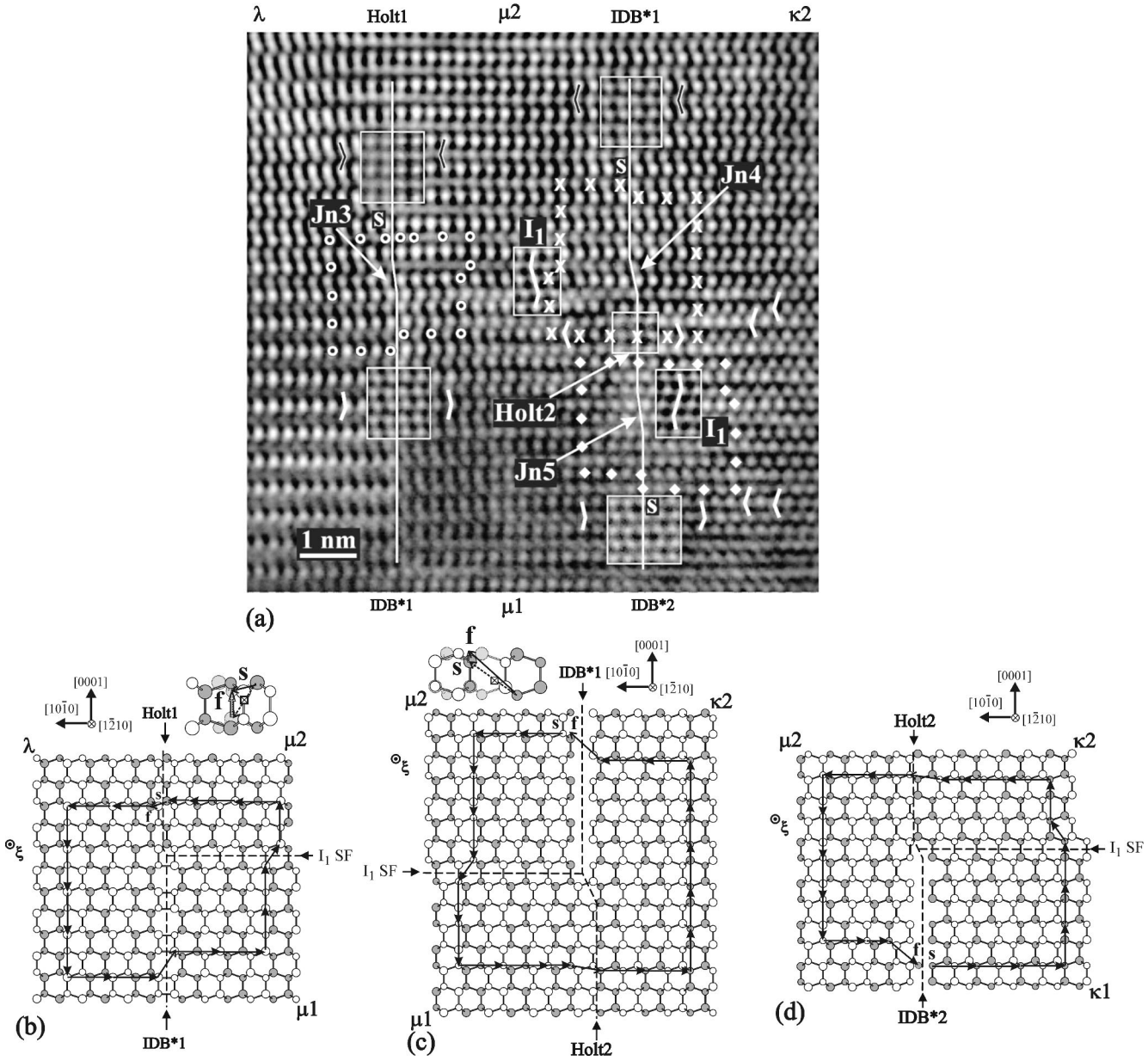

FIG. 12. (a) HREM micrograph depicting an inverse polarity domain with an internal I_1 SF that interacts with the two IDB's that bound the domain (junctions $Jn3$ and $Jn4$). On the right-hand image side, an external I_1 SF is seen also to interact with one domain wall (junction $Jn5$). The external SF terminates at a partial dislocation of mixed character with a $\frac{1}{2}[0001]$ screw component as indicated by the shift in the stacking sequence. Corresponding simulations of the IDB's are shown as framed insets. The relative orientations of the stacking sequences across the IDB's are also given (defocus$=-59$ nm, white spots represent the atomic columns and the IDB planes are on dark columns). Closed right-handed circuits have been drawn around the IDB-SF junction lines. (b), (c), and (d) Mappings of the circuits around $Jn3$, $Jn4$, and $Jn5$, respectively, to the reference space. Closure failures **fs** arise identifying these junction lines as partial dislocations with associated steps on the IDB plane (see text).

IDB wall or terminate there, remain to be further elucidated. Moreover, the transformation from a low energy planar defect to a high energy one should be influenced by kinetics. One explanation is the different growth rates exhibited by adjacent domains as has been shown in Refs. 7,9. A growth defect such as a I_1 SF could terminate on an IDB if an adjacent, unfaulted domain has already grown to a higher level, thus leading to a compulsory structural transformation of the IDB. This is because the I_1 SF cannot overcome the IDB since both glide and climb of the partial dislocation by which this SF is bounded would have been required. In a reverse procedure, a faulted domain may have grown to a higher level and the IDB structure transformation occurs as the adjacent inverse domain reaches the SF. As argued by Rouviere *et al.*,[7] Ga polarity domains grow faster than *N*-polarity ones, and hence such transformations could arise frequently. On the other hand, if there are two domains that have grown to the same level, the SF can cross the IDB wall.

We have observed this only at one instance where the inverse polarity domain was relatively narrow.

ACKNOWLEDGMENTS

This work was supported by the 99ED320 contract of the Greek General Secretariat of Research and Technology and by the HPRN-CT-1999-00040 contract of the European Union.

APPENDIX: CIRCUIT MAPPING METHODOLOGY

Circuit mapping is a useful technique for the characterization of line defects on experimental HREM micrographs. The method has been formulated by Pond and Hirth,[25] to utilize the mathematical framework of the *International Tables for Crystallography*,[29] and can employ all types of symmetry operations. Circuit mapping can be applied for the characterization of individual interfacial line defects and line defects at interface junction lines,[25,26] as has been demonstrated in a number of cases.[3,34–37]

In circuit mapping, an observer is imagined to undergo a closed excursion through the structure and around the line of the defect. Provided that he maintains sufficient distance from the defect core, his elementary motions can be perceived as symmetry operations. This circuit is then mapped to the appropriate reference space where a closure failure arises; for defects in single crystals the reference space is the space group of the host crystal. Under the rh/fs convention,[25] for a closed circuit that is right-handed with respect to the assigned line direction $\boldsymbol{\xi}$ of the defect, the defect is characterized by the vector **fs** connecting the finish location *f* to the starting one *s*.

The observer's excursion can be expressed mathematically in the form of a circuit operator $\mathcal{C}$.[25] This is particularly useful when employing operations that move the observer out of the projection plane, and when working in multicomponent systems such as bicrystals and polycrystals. The circuit operator is the sequence of symmetry operators undergone by the observer. However, since all symmetry operations are defined with respect to a chosen origin, action upon the observer by an operation $\mathcal{W}_i$ through any other location, defined by vector $\mathbf{r}_i$ with respect to this origin, is expressed as $\mathcal{W}_i^* = (\mathbf{I}, \mathbf{r}_i)\ \mathcal{W}_i (\mathbf{I}, \mathbf{r}_i)^{-1}$. Hence, the excursion is represented by the operator $\mathcal{C} = (\mathbf{C}, \mathbf{c}) = \mathcal{W}_n^* \cdots \mathcal{W}_1^*$. The circuit operator relates the final orientation and location of the observer to the original one. If **s** and **f** are the position vectors of locations *s* and *f*, respectively, with respect to the origin (i.e., $\mathbf{fs} = \mathbf{s} - \mathbf{f}$), then $\mathcal{C}(\mathbf{I}, \mathbf{s}) = (\mathbf{C}, \mathbf{Cs} + \mathbf{c})$ where $\mathbf{f} = \mathbf{Cs} + \mathbf{c}$ and **C** is the overall rotation and/or inversion of the observer's frame. Under the rh/fs convention, the defect is characterized by the operation $\mathcal{C}^{-1}$,[25] and we note that a more general sense of closure failure arises, i.e., a circuit is closed if the observer is returned to both his starting position and orientation. $\mathcal{C}^{-1}$ is the irreducible expression of the closure failure of the mapped excursion, provided that the circuit is closed in the general sense in real space.

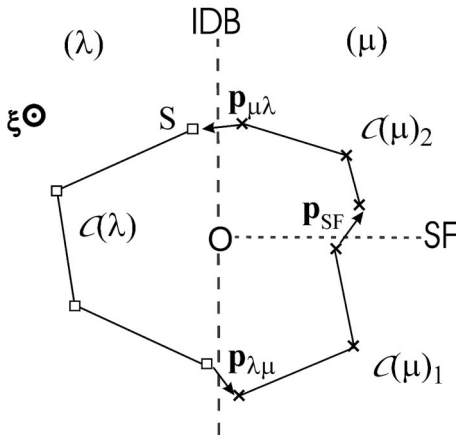

FIG. 13. Schematic illustration of a closed right-handed circuit employed in order to characterize the defect character of the junction line between an IDB and a terminating SF. The circuit, which is shown here prior to mapping to the reference space, starts at s in domain λ, and comprises three segments as well as translations associated with crossing the interfaces ($\vec{\xi}$ denotes the line direction of the defect).

For interfacial and junction line defects, more than one abutting crystal components are involved, and the circuit comprises segments in all components. The reference space is the space group of the composite complex that is formed if we imagine all component crystal structures to interpenetrate.[25,26] For example, consider the junction line of a SF with an IDB wall as illustrated schematically in Fig. 13. In order to identify the defect character of the interface junction line, we construct a circuit composed of segments, $\mathcal{C}(\lambda)$ in the λ domain, and $\mathcal{C}(\mu)_1$ and $\mathcal{C}(\mu)_2$, in the μ domain below and above the SF, respectively. The circuit also comprises displacements $\mathbf{p}_{\lambda\mu}$, $\mathbf{p}_{\mu\lambda}$, and $\mathbf{p}_{SF}$ associated with crossing the interfaces. For this junction line, the composite circuit operator is then given by the expression

$$\mathcal{C}(\lambda\mu) = (\mathbf{I}, \mathbf{p}_{\mu\lambda})\mathbf{P}\{\mathcal{C}(\mu)_2(\mathbf{I}, \mathbf{p}_{SF})\mathcal{C}(\mu)_1\}\mathbf{P}^{-1}, (\mathbf{I}, \mathbf{p}_{\lambda\mu})\mathcal{C}(\lambda). \tag{A1}$$

In Eq. (A1), the composite circuit operator is expressed in the λ coordinate frame, and $\mathbf{P} = \overline{\mathbf{1}}$. The term $\mathbf{P}\{\mathcal{C}(\mu)_2(\mathbf{I}, \mathbf{p}_{SF})\mathcal{C}(\mu)_1\}\mathbf{P}^{-1}$ reexpresses the μ circuit segments in the λ frame. Equation (A1) takes into account any structural transformation of the IDB type and yields the irreducible expression of the closure failure. A similar formulation can be written for the case that the SF crosses the IDB, as shown in Sec. III.

*Corresponding author. Electronic address: komnhnoy@auth.gr

[1] S. Nakamura, Science **281**, 956 (1998).

[2] H. Morkoç, S. Strite, G.B. Gao, M.E. Lin, B. Sverdlov, and M. Burns, J. Appl. Phys. **76**, 1363 (1994).

[3] V. Potin, P. Ruterana, G. Nouet, R.C. Pond, and H. Morkoç, Phys. Rev. B **61**, 5587 (2000).

[4] V. Potin, P. Ruterana, and G. Nouet, J. Phys.: Condens. Matter **12**, 10301 (2000).

[5] P. Ruterana and G. Nouet, Mater. Res. Soc. Symp. Proc. **595**, W5.4.1 (2000).
[6] X.H. Wu, L.M. Brown, D. Kapolnek, S. Keller, B. Keller, S.P. Den-Baars, and J.S. Speck, J. Appl. Phys. **80**, 3228 (1996).
[7] J.L. Rouviere, M. Arlery, R. Niebuhr, K.H. Bachem, and O. Briot, Mater. Sci. Eng., B **43**, 161 (1997).
[8] P. Vennegues, B. Beaumont, and P. Gibart, Mater. Sci. Eng., B **43**, 274 (1997).
[9] Ph. Komninou, Th. Kehagias, J. Kioseoglou, E. Sarigiannidou, Th. Karakostas, G. Nouet, P. Ruterana, K. Amimer, S. Mikroulis, and A. Georgakilas, Mat. Res. Soc. Symp. Proc. **639**, G3.47.1 (2001).
[10] Y. Xin, P.D. Brown, C.J. Humphreys, T.S. Cheng, and C.T. Foxon, Appl. Phys. Lett. **70**, 1308 (1997).
[11] J.E. Northrup, J. Neugebauer, and L.T. Romano, Phys. Rev. Lett. **77**, 103 (1996).
[12] J. Elsner, A. Th. Blumenau, Th. Frauenheim, R. Jones, and M. I. Heggie, Mat. Res. Soc. Symp. Proc. **595**, W9.3.1 (2000).
[13] E.S. Hellman, MRS Internet J. Nitride Semicond. Res. **3**, 11 (1998).
[14] B. Daudin, J.L. Rouviere, and M. Arlery, Mater. Sci. Eng., B **43**, 157 (1997).
[15] V. Potin, G. Nouet, and P. Ruterana, Appl. Phys. Lett. **74**, 947 (1999).
[16] V. Potin, G. Nouet, and P. Ruterana, Philos. Mag. A **79**, 2899 (1999).
[17] B. Pecz, M.A. di Forte-Poisson, F. Huet, G. Radnoczi, L. Toth, V. Papaioannou, and J. Stoemenos, J. Appl. Phys. **86**, 6059 (1999).
[18] D. Cherns, W.T. Young, M. Saunders, J.W. Steeds, F.A. Ponce, and S. Nakamura, Philos. Mag. A **77**, 273 (1998).
[19] D.B. Holt, J. Mater. Sci. **19**, 439 (1984).
[20] C. Stampfl and C.G. Van de Walle, Phys. Rev. B **57**, R15 052 (1998).
[21] P. Ruterana, V. Potin, B. Barbaray, and G. Nouet, Philos. Mag. A **80**, 937 (2000).
[22] Ph. Komninou, J. Kioseoglou, E. Sarigiannidou, G. P. Dimitrakopulos, Th. Kehagias, A. Georgakilas, G. Nouet, P. Ruterana, and Th. Karakostas, Mat. Res. Soc. Symp. Proc. **639**, G3.44.1 (2001).
[23] R. C. Pond, in *Dislocations in Solids*, Vol. 8, edited by F. R. N. Nabarro (North Holland, Amsterdam, 1989).
[24] F.C. Frank, Philos. Mag. **42**, 809 (1951).
[25] R.C. Pond and J.P. Hirth, Solid State Phys. **47**, 288 (1994).
[26] G.P. Dimitrakopulos, Th. Karakostas, and R.C. Pond, Interface Sci. **4**, 129 (1996).
[27] G.P. Dimitrakopulos, Th. Karakostas, J.G. Antonopoulos, and R.C. Pond, Interface Sci. **5**, 35 (1997).
[28] V. Volterra, Ann. Sci. Ec. Norm. Sup. Paris **24**, 401 (1907).
[29] *International Tables for Crystallography*, edited by T. Hahn (Reidel, Dordrecht, 1983).
[30] J. P. Hirth and J. Lothe, *Theory of Dislocations*, 2nd ed. (Wiley, New York, 1982), p. 345.
[31] S.B. Austerman and W.G. Gehman, J. Mater. Sci. **1**, 249 (1966).
[32] P.A. Stadelmann, Ultramicroscopy **21**, 131 (1987).
[33] R. Serneels, M. Snykers, P. Delavignette, R. Gevers, and S. Amelinckx, Phys. Status Solidi **58**, 277 (1973).
[34] R.C. Pond, Interface Sci. **2**, 299 (1995).
[35] G.P. Dimitrakopulos, Ph. Komninou, Th. Karakostas, and R.C. Pond, Interface Sci. **7**, 217 (1999).
[36] A.N. Kiselev, F. Sarrazit, E.A. Stepantsov, E. Olsson, T. Claeson, V.I. Bondarenko, R.C. Pond, and N.A. Kiselev, Philos. Mag. A **76**, 633 (1997).
[37] T. Braisaz, P. Ruterana, G. Nouet, A. Serra, P. Komninou, T. Kehagias, and T. Karakostas, Philos. Mag. Lett. **74**, 331 (1996).